

Removing scanner biases using Generative Adversarial Networks

Harrison Nguyen^a, Richard W. Morris^{b,c}, Anthony W. Harris^{b,d}, Mayuresh S. Korgoankar^{b,d}, Fabio Ramos^{a,c,*}

^a*School of Information Technologies, University of Sydney, Sydney, Australia*

^b*School of Medicine, University of Sydney, Sydney, Australia*

^c*Centre for Translational Datascience, University of Sydney, Sydney, Australia*

^d*Brain Dynamics Centre, Westmead Millennium Institute, Sydney, Australia*

Abstract

Magnetic Resonance Imaging (MRI) of the brain has been used to investigate a wide range of neurological disorders, but data acquisition can be expensive, time-consuming, and inconvenient. Multi-site studies present a valuable opportunity to advance research by pooling data in order to increase sensitivity and statistical power. However images derived from MRI are susceptible to both obvious and non-obvious differences between sites which can introduce bias and subject variance, and so reduce statistical power. To rectify these differences, we propose a data driven approach using a deep learning architecture known as generative adversarial networks (GANs). GANs learn to estimate two distributions, and can then be used to transform examples from one distribution into the other distribution. Here we transform T1-weighted brain images collected from two different sites into MR images from the same site. We evaluate whether our model can reduce site-specific differences without loss of information related to gender (male, female) or clinical diagnosis (schizophrenia, bipolar disorder, healthy). When trained appropriately, our model is able to normalise imaging sets to a common scanner set with less information loss compared to current approaches. An important advantage is our method can be treated as a black

*Corresponding author

Email address: fabio.ramos@sydney.edu.au (Fabio Ramos)

URL: <https://sydney.edu.au/engineering/people/fabio.ramos.php> (Fabio Ramos)

box that does not require any knowledge of the sources of bias but only needs at least two distinct imaging sets.

Keywords: Structural MRI, Classification, Deep learning, Generative Adversarial Network, Support Vector machines, Between-scanner variability

1. Introduction

One of the biggest challenges in the translation of neuroimaging findings into clinical practice is the need to validate models across large independent samples and across data obtained from different MRI scanners. Combining multiple samples increases the overall sample size, overcoming a limitation common to many neuroimaging studies. However it also introduces heterogeneity into the sample from differences in scanner manufacturer, MRI protocol, variation in site thermal and power stability, and gradient linearity, centering and eddy currents. Therefore, images from different scanners and sites have the potential to introduce bias that can either mimic or obscure true changes or even worse, produce results that could be driven by the artifactual site differences. This can make the interpretation, reliability and reproducibility of findings difficult. Despite these issues, pooling data provides the opportunity to address a major source of concern regarding the low statistical power of published studies, especially when larger studies are not feasible due to financial constraints or recruitment is difficult because a particular disorder is rare at a specific geographical location (Poldrack & Gorgolewski, 2014).

Given the considerable incentives to pool data, there is a relative paucity of methods available to correct for site-specific differences in MR images. The majority of approaches are usually applied during data acquisition, for instance, using a common phantom across sites to calibrate and reduce differences in field homogeneities. However, these *a priori* methods require careful planning and are not applicable to data sets that have already been collected or other *post hoc* forms of data pooling. Site differences can also be addressed in a *post hoc* fashion by treating the site as a covariate in the analysis for evaluation

of confounding effects. However, the interaction between the usually unknown site-specific effects and the true brain effects on the MRI signal seem to be highly complex and nonlinear such that the inclusion of the covariate can also introduce bias (Rao et al., 2017).

Recent advances in computer vision due to the application of artificial neural networks suggests there may be a novel *post hoc* solution to remove non-linear bias in MR images. For example, superior performance in non-linear, multi-variate pattern classification problems such as Alzheimers disease classification, brain lesion segmentation, skull stripping and brain age prediction have been achieved using deep learning networks (Payan & Montana, 2015; Sarraf et al., 2016; Kamnitsas et al., 2017; Kleesiek et al., 2016; Cole et al., 2017). Deep learning provides some unique advantages for high-dimensional data such as MRI data, since it does not require extensive feature engineering. Furthermore, deep learning has produced important advances in generative modeling. Generative modeling involves learning to estimate a given distribution in order to produce examples from that distribution. For example, after being trained on a set of images, the model is able to generate a new, unseen sample from the training set. Generative modeling is considered a much more difficult task than pattern classification, as the output of these models are typically high dimensional and a single input may correspond to many correct answers (e.g. there are many ways of producing an image of a cat).

One class of generative models, known as generative adversarial networks (GANs), have recently recently achieved considerable success in a variety of image problems, from image generation (Radford et al., 2015), super resolution generation (Ledig et al., 2016), text2image (Reed et al., 2016) and image-to-image translation (Isola et al., 2016) (See Figure 1 for examples). GANs succeed through the idea of adversarial training, where the models training process can be described as a game between two players. One player is called the generator where it attempts to create samples from the same distribution as the observed data. The other player is the discriminator where its function is to examine the fake samples from the generator and real samples from the observed data and

to classify the generated and observed samples as either real or fake. Over time, the discriminator is trained with supervision to better distinguish real and fake samples. However at the same time, the generator will improve its synthesis of fake samples in order to fool the discriminator, which in turn will make the job of the discriminator more difficult. Eventually the solution of this game is a Nash equilibrium, where the generator is unable to improve its generation of fake samples and the discriminator is unable to better classify real and fake samples (Goodfellow, 2016). See Box 1 for further details.

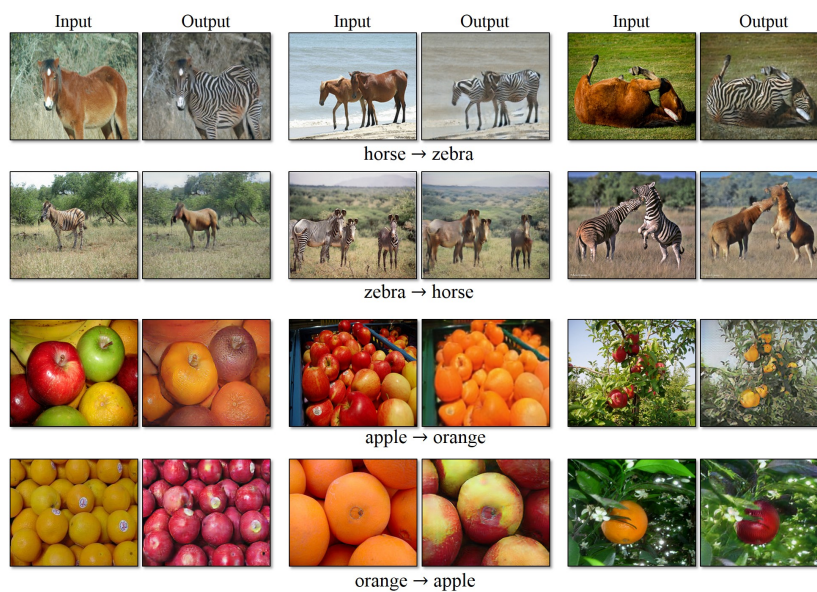


Figure 1: Examples of images produced from CycleGAN (Zhu et al., 2017). Published without permission.

Here, we propose an algorithm that uses GANs to transform a set of images from a given MR scanner into images with characteristics of a different MR scanner. Its purpose is to correct for differences in scanner artifacts without the need for *a priori* calibration using phantoms or significant coordination of acquisition parameters. This algorithm can be treated as a black box without knowledge of the artifacts present in the dataset and can be applied *post hoc*

after acquisition to two or more unpaired sets of imaging data. Importantly, as we demonstrate, the correction occurs without any apparent loss of information related to gender or clinical diagnosis.

2. Material and methods

2.1. Participants

Structural (T1-weighted) MR brain images were obtained ($N = 358$) from pre-existing MRI studies conducted at two different sites (site A and site B). The cohort from each site contained two diagnostic groups (schizophrenia and healthy adults), however these groups were not evenly distributed over sites (see Table 1). All clinical cases met DSM-IV criteria for their disorder with no other Axis I disorders, on the basis of either the Mini-International Neuropsychiatric Interview (Sheehan et al., 1998) or the Structured Clinical Interview for DSM-IV Axis I and II Disorders (First, Spitzer, Gibbon, Williams, 2002). Participants were aged 18-65 years and spoke fluent English. Exclusion criteria included the presence of an organic brain disorder, brain injury with post-traumatic amnesia, mental retardation (WAIS-III IQ score less than 80), movement disorders and recent (within 6 months) substance dependence or electroconvulsive therapy. Healthy adults were also screened for the absence of personal or family history of any DSM-IV Axis I disorder.

2.2. MR Scanner, image data and preprocessing

Data were collected on two different MR scanners: a Phillips Achieva 3T with a 8-channel headcoil and receiver (NeuRA, Randwick NSW, Australia); and a GE Discovery MR750 3T with a 8-channel headcoil and receiver (Brain and Mind Centre, Camperdown NSW, Australia). T1-weighted image volumes were acquired using a standard but scanner-specific MPRAGE acquisition sequence. T1 images from site A were acquired with a 3D Fast Spoiled Gradient Recall Echo (FSPGR) sequence with SENSE acceleration; 8.3-ms TR, 3.2-ms TE; and 11 degree flip angle, and comprised of 180 sagittal 1-mm slices in a 256 x 256

Table 1: Subject and gender distribution across sites (Age mean is reported with one SD. m:male, f:female)

	Site A (n=58)	Site B (n=255)	Total (n=313)
Control			
age \pm SD	29.7 \pm 13.1	31.2 \pm 8.7	31.2 \pm 10.1
m/f	23/18	52/49	75/67
Schizophrenia			
age \pm SD	44.8 \pm 11.1	38.0 \pm 9.5	38.7 \pm 9.8
m/f	7/10	57/97	64/107
Total			
age \pm SD	34.1 \pm 14.1	35.3 \pm 9.7	35.1 \pm 10.7
m/f	30/28	109/158	139/174

matrix (1 mm isotropic voxel dimensions). Images from site B were acquired with a 3D Turbo Field Echo sequence (TFE) with ASSET acceleration; 7.192-ms TR, 2.732-ms TE; and 12 degree flip angle, and comprised of 176 sagittal 1-mm slices in a 256 x 256 matrix (1 mm isotropic voxel dimensions).

After checking for scanner artifacts and gross anatomical abnormalities for each image, we reoriented the original images along the anterior-posterior commissure (AC-PC) line and set the AC as the origin of the spatial coordinates to assist the normalization algorithm. The segmentation procedure implemented in SPM12 (<http://www.fil.ion.ucl.ac.uk/spm>), running under Matlab 8.4 (Math Works, Natick, MA, USA) was used to segment all the images into gray matter (GM), white matter (WM) and cerebrospinal fluid (CSF) space, i.e. maps of probability values representing the probability of a voxel containing a specific tissue type. A fast diffeomorphic image registration algorithm (DARTEL; Ashburner, 2007) was used to warp the GM partitions into a new study-specific reference space representing an average of all the subjects included in the analysis. As an initial step, a set of study-specific templates and the corresponding deformation fields, required to warp the data from each subject to the new refer-

ence space, were created using the GM partitions (Ashburner and Friston, 2009). Each subject-specific deformation field was used to warp the corresponding GM partition into the new reference space with the aim of maximizing accuracy and sensitivity (Yassa and Stark, 2009); the warped GM partitions were affine transformed into the MNI space and an additional modulation step was used to scale the GM probability values by the Jacobian determinants of the deformations in order to ensure that the total amount of gray matter in each voxel was conserved after the registration (Ashburner and Friston, 2000; Good et al., 2001; Mechelli, Friston, Frackowiak, and Price, 2005). After this preprocessing, we obtained modulated, normalized grey matter density maps, from which we extracted the middle five 2D sagittal slices to be used to train the GAN model.

2.3. Generative Adversarial Networks

Notation: In the following, we have defined capital bold font, \mathbf{X} , as a matrix or a set of images and lower case bold font, \mathbf{x} , as a vector or one example image. G_θ , D_ϕ denotes a mapping function parameterised by θ and ϕ , respectively. $P(\mathbf{X})$ indicates the probability distribution for the imaging set \mathbf{X} , and $\hat{P}(\mathbf{X})$ is an estimate of that probability distribution.

Rather than removing scanner artifacts and biases from the set of sMRI images, we seek to transform one set of images from a scanner to images that come from the distribution of images of another scanner, while still preserving the important features of the original images. The problem at hand can be described as image-to-image translation in the computer vision literature where the goal is to learn a mapping function between a set of MRI images from domain \mathbf{X} and another set of images from domain \mathbf{Y} ; learn $G : \mathbf{X} \rightarrow \mathbf{Y}$ such that $G(\mathbf{x})$ for each $\mathbf{x} \in \mathbf{X}$ is indistinguishable from the set of images from domain \mathbf{Y} .

The CycleGAN (Zhu et al., 2017) and DiscoGAN (Kim et al., 2017) have been developed to learn cross domain relationships between sets of natural objects such as from horses to zebras, edges to photos and Monet artworks to realistic photos. The advantage of these models is that they do not require paired sets of training samples, $\{\mathbf{x}_i, \mathbf{y}_i\}_{i=1}^N$, which is often difficult to obtain

for neuro-imaging data, and instead only require unpaired imaging data consisting of a source set $\{\mathbf{x}_i\}_{i=1}^N \in \mathbf{X}$ and target set $\{\mathbf{y}_j\}_{j=1}^M \in \mathbf{Y}$, without any \mathbf{x}_i 's necessarily corresponding to any \mathbf{y}_j 's. These models attempt to transform the underlying distribution of $P(\mathbf{X})$ to an estimate of $P(\mathbf{Y})$, $\hat{P}(\mathbf{Y})$, through G while still preserving the important features of the original sample, \mathbf{x}_i , but also merging these with the particular characteristics of $P(\mathbf{Y})$.

To learn this mapping function, an adversarial training regime was utilised using the GAN formulation. The generator, G_θ , represented as a convolutional neural network defined by parameters θ , takes as input, images from \mathbf{X} and transforms these images, $G_\theta(\mathbf{x})$, as if they were sampled from $P(\mathbf{Y})$. The discriminator, D_ϕ on the other hand, is a supervised classifier represented as a convolutional neural network. The discriminator observes two inputs, the observed images from \mathbf{Y} and generated samples $G_\theta(\mathbf{x})$. The goal of the discriminator is to output a probability that its inputs are either real or fake, with the true labels being observed samples as real and generated samples as fake. The discriminator attempts to learn that its output from samples of \mathbf{Y} , $D_\phi(\mathbf{y})$, are given to be given values near 1 and inputs from the generator, $D_\phi(G_\theta(\mathbf{x}))$, to be values close to 0. However, at the same time, the generator will attempt to make the quantity, $D_\phi(G_\theta(\mathbf{x}))$ to approach 1. At equilibrium, $D_\phi(\mathbf{y}) = \frac{1}{2}$ for all \mathbf{y} and $G_\theta(\mathbf{x})$ which means that the discriminator is unable to distinguish between real and generated samples.

The generator and discriminator face two competing objectives during training; the discriminator attempts to push $D_\phi(G_\theta(\mathbf{x}))$ to 0 and whilst on the other hand, the generators strives to fool the discriminator and make $D_\phi(G_\theta(\mathbf{x}))$ equal to 1.

More specifically, the Least Squares GAN (LSGAN) (Mao et al., 2016) is used to train the discriminator and generator, where the discriminator's objective function is

$$\min_{\phi} \frac{1}{2} E_{\mathbf{y} \sim p(\mathbf{Y})} [(D_\phi(\mathbf{y}) - 1)^2] + \frac{1}{2} E_{\mathbf{x} \sim p(\mathbf{X})} [(D_\phi(G_\theta(\mathbf{x})))^2], \quad (1)$$

and the generator competes against the discriminator by having the objective

function

$$\min_{\theta} \frac{1}{2} E_{\mathbf{x} \sim p(\mathbf{x})} [(D_{\phi}(G_{\theta}(\mathbf{x})) - 1)^2]. \quad (2)$$

Equation 1 and 2 is typically optimised using stochastic gradient descent where ϕ is updated keeping the generator’s parameters fixed for one or more iterations and vice versa. Details about the training parameters are described in Section 2.4. Equation 1 is optimised in a supervised manner where the ground truth labels, real or fake, are provided to the discriminator through the inputs \mathbf{y} and $G_{\theta}(\mathbf{x})$ respectively. Mao et al. demonstrated that minimising the objective function of LSGAN yields minimising the Pearson χ^2 divergence between \mathbf{Y} and $G_{\theta}(\mathbf{x})$ (Mao et al., 2016).

Equation 2, in contrast to the learning objective of the discriminator, shows the generator does not have the same level of supervision as the discriminator. While although they have competing objectives, the generator improves its generation of samples, not because of the directive by a supervisor but rather, by the information provided by the discriminator. It is through the cooperation between the generator and discriminator that the generator learns the mapping function in an unsupervised manner. This enables the ability to learn the transformation that is data driven and without any a-priori knowledge of the processes that generated the two image sets.

The GAN objectives is not limited to Equations 1 and 2. Other adversarial formulations have been developed in order to minimise other divergence measures between the observed distribution and generated distribution such as the f -divergence (Nowozin et al., 2016), Jensen-Shannon divergence (Goodfellow, 2016) or other distance metrics to have different geometric interpretations such as, and not limited to, Earth Mover distance (Arjovsky et al., 2017) and Integral Probability Metrics (Mroueh et al., 2017). Results based on the f -divergence, Jensen-Shannon divergence and Earth Mover distance were also included in experiments but produced similar results to the LSGAN. They have not been included for the sake of brevity.

2.3.1. Cycle loss

However, the transformation $G : \mathbf{X} \rightarrow \mathbf{Y}$ is ill-posed as there are infinitely many mappings, $G(\mathbf{x})$, that could induce the estimated distribution $\hat{P}(\mathbf{Y})$. This means that each \mathbf{x} and output $G(\mathbf{x})$ do not necessarily have to have any meaningful relationship. For example, a possible outcome is that G_θ learns to transform all $\mathbf{x} \in \mathbf{X}$, to only one particular example of \mathbf{Y} . This outcome is known as mode collapse where the generator learns to map several different input values to the same output point that fools the discriminator and the model is unable to make any progress in training.

To prevent this issue from occurring, the model is required to be constrained to a one-to-one correspondence (bijective mapping) by introducing the idea of a *cycle* loss (Zhu et al., 2017). If we have a mapping $G : \mathbf{X} \rightarrow \mathbf{Y}$ and another mapping $F : \mathbf{Y} \rightarrow \mathbf{X}$ then G and F should be inverses of each other. To ensure this, the generators G and F are both trained simultaneously with their own adversarial loss and own parameters, θ_1 and θ_2 respectively but also adding a loss that encourages $F_{\theta_2}(G_{\theta_1}(\mathbf{x})) \approx \mathbf{x}$ and $G_{\theta_1}(F_{\theta_2}(\mathbf{y})) \approx \mathbf{y}$. The generators G_{θ_1} and F_{θ_2} are able to reconstruct the original set of images. Any distance metric function (L_1 , Huber loss, cosine) could be used but in particular, the L_2 norm was used,

$$L_{cycle}(G, F) = E_{\mathbf{x} \sim p(\mathbf{X})}[\|F_{\theta_2}(G_{\theta_1}(\mathbf{x})) - \mathbf{x}\|_2] + E_{\mathbf{y} \sim p(\mathbf{Y})}[\|G_{\theta_1}(F_{\theta_2}(\mathbf{y})) - \mathbf{y}\|_2]. \quad (3)$$

2.3.2. Full objective

The model contains two pairs of GANs, with each generator learning the respective mapping functions $G : \mathbf{X} \rightarrow \mathbf{Y}$ and $F : \mathbf{Y} \rightarrow \mathbf{X}$. Each generator will have their respective discriminators, D_{ϕ_1} and D_{ϕ_2} , where D_{ϕ_1} will discriminate between $\mathbf{x} \in \mathbf{X}$ and samples from F_{θ_2} and conversely, D_{ϕ_2} will distinguish between $\mathbf{y} \in \mathbf{Y}$ and the output of G_{θ_1} . The objective function of G_{θ_1} and D_{ϕ_2}

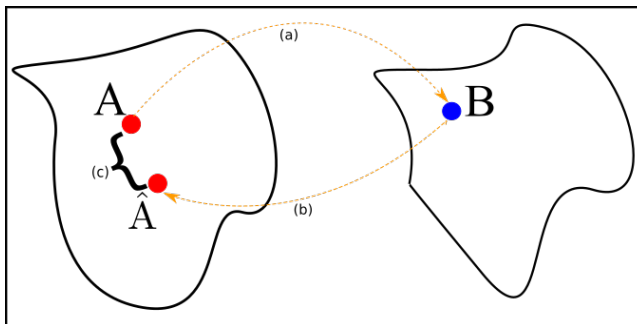


Figure 2: **(a)**: Image A is mapped into the manifold of scanner set B through a a convolutional neural network (generator). **(b)**: This image is then transformed back to the original manifold to reconstruct the original image using a different CNN. **(c)**: The original and reconstructed image is compared using some distance metric (e.g. L_1 or L_2 -norm).

is given respectively as

$$\min_{\theta_1} E_{\mathbf{x} \sim p(\mathbf{X})} [(D_{\phi_2}(G_{\theta_1}(\mathbf{x})) - 1)^2] + \lambda L_{cycle}(G_{\theta_1}, F_{\theta_2}) \quad (4)$$

$$\min_{\phi_2} E_{\mathbf{y} \sim p(\mathbf{Y})} [(D_{\phi_2}(\mathbf{y}) - 1)^2] + E_{\mathbf{x} \sim p(\mathbf{X})} [(D_{\phi_2}(G_{\theta_1}(\mathbf{x})))^2] \quad (5)$$

where λ is a constant that controls the relative importance between the adversarial loss and reconstruction loss. The objective function for F_{θ_2} and D_{ϕ_1} are similarly defined.

2.4. Implementation

The generators and discriminators are fully convolutional neural networks. The discriminators are composed of six convolutional layers to create a receptive field of 30×30 patches that aims to classify whether 30×30 overlapping image patches are either real or fake. The transformations of the input consists of a succession of spatial 2D convolutions, a transformation that keeps the input distribution of each hidden layer similar during training by normalising a training batch (batch normalisation) and a voxel-wise non-linear transformation (also known as an activation function) of the results of the convolutions.

During training, the input distribution of each hidden layer may change after several iterations, known as internal covariate shift, due to the complicated non-linearities of the incoming neurons. The current hidden layers will have to continually adapt to these changes in the input distribution hence could slow down convergence. Batch normalisations attempts to rectify this by normalising the inputs to each hidden layer so that their distribution during training remains fairly constant (Ioffe & Szegedy, 2015) which improves convergence of training. In regards to the choice of activation function, the *leakyReLU* activation function was used as it was found to have the best qualitative performance except in the last layer of the discriminators where no activation function was used.

The generators contain two convolutional down sampling layers, reducing the dimensionality of the image by a factor of four, followed by six residual blocks to create new features of the data then another two convolutional upsampling layers to restore the image back to the original input dimensions. The residual blocks is composed of two convolutional layers that includes a 'skip' connection, where the input to these layers are added to the output of the convolution layers. The residual blocks are critical to the generator as some portions of the image may not necessarily require any transformations. Therefore, including these residual layers will give the option of the network to skip convolutional layers and not undergo any change. Much like the discriminator, each convolutional layer is followed by batch normalisation and then a *leakyReLU* activation function. However, the last layer of the generator uses a *tanh* function that scales the output from -1 to 1, producing a new grey matter voxel map. More specific details about the architecture used is found in Table 2.

During training, mini-batches consisting of eight sagittal slices were constructed from each scanner set. The filters of the CNN were initialised as described by Glorot and Bengio (Glorot & Bengio, 2010). The network was trained using Adam optimisation (Kingma & Ba, 2014) with a starting learning rate of $2e-4$ for the generators and discriminators. The generators and discriminators were trained concurrently; every one gradient step of the generator was taken

(a) Architecture of Generator

Layer	Layer Type	No. of Filters	Stride	Batch Norm	Activation Function
1	Convolution	32	2	No	LeakyReLU
2	Convolution	64	2	Yes	LeakyReLU
3	Convolution	128	2	Yes	LeakyReLU
4-6	Residual Block	128	1	Yes	LeakyReLU
7	Convolution Transpose	64	2	Yes	LeakyReLU
8	Convolution Transpose	32	2	Yes	LeakyReLU
9	Convolution	1	1	No	Tanh

(b) Architecture of Discriminator

Layer	Layer Type	No. of Filters	Stride	Batch Norm	Activation Function
1	Convolution	64	2	No	LeakyReLU
2	Convolution	128	2	Yes	LeakyReLU
3	Convolution	256	2	Yes	LeakyReLU
4	Convolution	256	1	Yes	LeakyReLU
5	Convolution	256	1	Yes	LeakyReLU
6	Convolution	1	1	No	None

Table 2: Architecture of Generative Neural Network

with the discriminator parameters fixed followed by a gradient step of the discriminator, keeping the generator parameters fixed. Training was stopped when the cycle loss (Equation 3) failed to stop decreasing. It was found empirically that the hyperparameter, λ , in Equation 4 was set to $\lambda = 0.2$, balancing between faster convergence and qualitative results.

2.5. Postprocessing

For better classification results as outlined in Section 2.8, transformations obtained from the GAN model were centred to mean 0 and Principal Component Analysis (PCA) was used to transform the data into orthogonal eigenvector components, ordered according to their contribution of variation in explaining the dataset. The first 50 components was used as features to train the supervised learning models.

2.6. Support vector machine classification

The GAN correction method was evaluated by the improvement of a learned supervised classifier in a range of problems such as scanner, gender and disease classification. This evaluation method was used because of the lack of ground truth; there were a limited number of subjects who were scanned across the two centres in similar conditions. Supervised binary classification learns a decision boundary based on a data set of labeled examples $\mathcal{D} = \{(\mathbf{x}_i, y_i)\}, i = 1, \dots, N$, where $x_i \in \mathbb{R}^D$ is the input data and $y_i \in \{-1, 1\}$ is the binary class label. A popular technique for the classification of high dimensional data with limited examples is the support vector machine (SVM). It has been used for classification of many neurological diseases such as Alzheimer’s Disease (Magnin et al., 2009; Jongkreangkrai et al., 2016), Huntington’s Disease (Kostro et al., 2014) and mental illnesses (Sacchet et al., 2015). SVMs learn a decision boundary based on labeled examples by maximising the margin between training examples and minimising the norm of the solution vector $\hat{\mathbf{w}}$,

$$\min_{\mathbf{w}} \frac{1}{n} \sum_{i=1}^n \max(0, 1 - y_i(\mathbf{w} \cdot \mathbf{x}_i - b)) + \lambda \|\mathbf{w}\|^2, \quad (6)$$

where the parameter $\lambda > 0$ determines the tradeoff between increasing the margin-size and ensuring that \mathbf{x}_i lies of the correct side of the margin. Optimising Equation 6 can be rewritten as a constraint optimisation problem with a differentiable objective function in the following way, called the primal problem,

$$\min \frac{1}{n} \sum_{i=1}^n \zeta_i + \lambda \|\mathbf{w}\|^2$$

subject to $y_i(\mathbf{w} \cdot \mathbf{x}_i - b) \geq 1 - \zeta_i$ and $\zeta_i \geq 0$, for all i . (7)

The grey matter concentrations of each voxel was used as input for the classification. The primal solution, $\hat{\mathbf{w}}$, when using a linear SVM, is a linear combination of the input voxels and hence the spatial patterns of voxels that were relevant for the classification process can be visualised.

2.7. Regression based correction methods

The performance of the GAN correction was compared against two other popular *post-hoc* correction methods: linear regression and Gaussian Process (GP) regression, which have previously been used to compensate for non-disease specific effects (Kostro et al., 2014; Rao et al., 2017; Dukart et al., 2011).

A regression model was learned to estimate the GM density for every voxel based on examples of subject-specific covariate and their corresponding GM density maps. The general linear model for the voxels is given as

$$\mathbf{y} = \mathbf{X}\beta + \epsilon, \epsilon \sim \mathcal{N}(0, \sigma^2), \tag{8}$$

where \mathbf{y} is a $N \times v$ matrix, where the columns represent the observed GM concentrations of each voxels and the rows are the observations of each of the N control subjects. $\mathbf{X} \in \mathbb{R}^{N \times 1}$ is the design matrix representing the subjects' scanner characteristic, coded as $\{0, 1\}$. $\beta \in \mathbb{R}^{1 \times v}$ represents the effect strengths associated to the scanner for each voxel. The regression parameters β were estimated for each voxel independently with only the control subjects. The model was applied to new data, $\mathbf{x}^{(*)}$, to obtain a subject specific template, and was subtracted from the observed GM map to get a corrected image.

$$\hat{\mathbf{y}}_{OLS}^{(*)} = \mathbf{y}^{(*)} - \mathbf{x}^{(*)}\hat{\beta}. \tag{9}$$

where $\hat{\mathbf{y}}_{OLS}^{(*)}$ is the corrected GM map of the original, $\mathbf{y}^{(*)}$ of the test example.

The GP regression correction method is analogous to Equation 9.

$$\hat{\mathbf{y}}_{GPR}^{(*)} = \mathbf{y}^{(*)} - (\mathbf{k}_\theta^{(*)})^T \mathbf{K}_\theta^{-1} \mathbf{y}. \quad (10)$$

$\hat{\mathbf{y}}_{GPR}^{(*)}$ and $\mathbf{y}^{(*)}$ are the corrected and original images respectively. \mathbf{K}_θ is the covariance kernel matrix of the training examples with the elements corresponding to the output of the kernel function $k_\theta(\mathbf{x}_i, \mathbf{x}_j)$, for $i, j \in \{1, \dots, N\}$. The coefficients of the regression, $\mathbf{k}_\theta^{(*)}$, is the kernel function values of the test example with all the training examples. The kernel used was similar to [Kostro et al. \(2014\)](#) where the covariance between the input images \mathbf{x}_i and \mathbf{x}_j was

$$k_{\theta, \sigma}(\mathbf{x}_i, \mathbf{x}_j) = \theta_1^2 \exp(-\theta_2^2 (\mathbf{x}_i - \mathbf{x}_j)^2) + \theta_3^2 + \theta_4^2 (\mathbf{x}_i)^T \mathbf{x}_j + \sigma^2 \delta_{ij}, \quad (11)$$

where $\theta_k, k = \{1, \dots, 4\}$ and σ are scalar model hyperparameters, and δ_{ij} is the delta function; one if $i = j$ and zero, otherwise. The optimal hyperparameters were determined by maximising the likelihood function.

2.8. Evaluation methods

The effectiveness of each correction technique (linear regression, GP regression and GAN) was assessed by the classification performance of a Gaussian kernel SVM. Accuracy, precision and recall of the learned SVM was evaluated using 10-fold cross validation after each correction method was applied to the dataset, as well as a baseline of no correction. For robust evaluation, the results reported were obtained in the following manner: for a test fold, the performance measure (accuracy, precision, recall and specificity) was computed for each of the correction methods and baseline. The difference of each measure was taken between baseline and the correction method. This was repeated for every test fold, collecting 10 sample sets for each method in each experiment. The average and standard deviation over the 10 sample sets was calculated for each method, and are the values reported. Significant differences in performance between each correction method and baseline were then compared by *t*-test with Rodger’s correction to control the type-I error rate at $\alpha = 0.05$.

Box 1: Simulation with MNIST

The MNIST contains 50000 training examples of handwritten digits between 0 and 9. The training and test set was split in half, with one half being unaltered (Figure 3 top row) and the other half was change to have a black written digit against a white background, corrupted with Gaussian noise (Figure 3 second row).

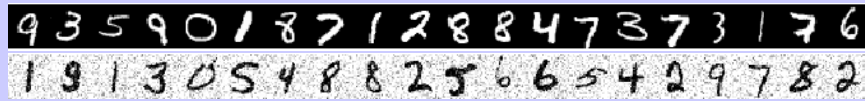


Figure 3: Sample of MNIST data set used for training

A GAN was trained to transform the normal images to corrupted images and vice versa. The training procedure is demonstrated in Figure 4.

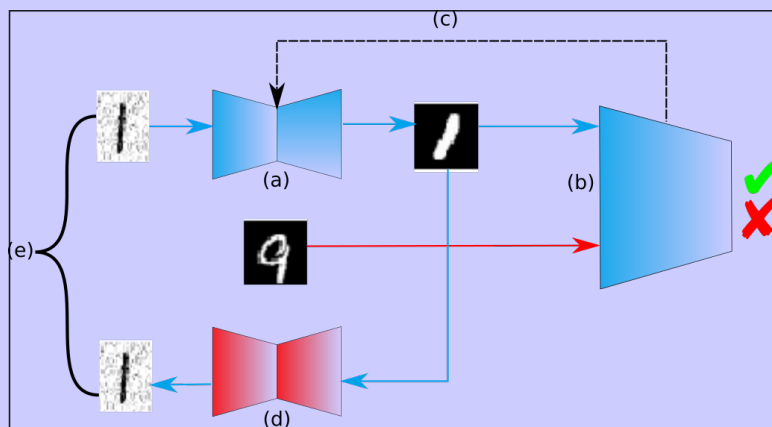


Figure 4

(a) A generator attempts to transform a corrupted images into a normal image. Since the generator has been initialised with random weights, in the beginning, it produces a random (noisy) image. (b) A discriminator attempts to classify the transformed images as fake and another image from other set as real. The digits do not necessarily have to correspond to each other. (c) The classification of the discriminator is used as information to update the generator's parameters. The discriminator, on the other hand,

is told which image is fake or real and thus, is trained through supervised learning. (d) Another generator takes transformed image and attempts to reconstruct original image. (e) The original image and reconstructed image is compared and the reconstruction error is used to update both generators' parameters. (f) This process is mirrored for the other set of images using the same respective generators but a different discriminator.

Therefore in each training cycle, the generators undergo two passes, one to transform a real image into a fake image and another to reconstruct a fake image into the original. As training progresses, the generator gradually improves its generation of images in order to fool the discriminator. At convergence, the generator is no longer able to fool the discriminator, and the discriminator is no longer able to distinguish between the observed and generated data.

Figure 5 show the result of the GAN transformations on an unseen test set. These images demonstrate that the transformation still maintains the input images' most important information, its digit, and at the same time, is able to add characteristics that define the two sets of images. The GAN is able to denoise images (compare the bottom row of Figure 3 and 5) but is also able to deterministically include features that look like Gaussian noise (compare the top row).



Figure 5: Transformed MNIST images

3. Results

3.1. Experiment 1a: Supervised classification test of scanner

To illustrate the confounding influence of scanner bias on the ability to classify clinical diagnosis in our dataset, we initially performed a disease classification on our original full dataset. Our full dataset contained images from

two different groups and two different scanners. A polynomial SVM indicated the diagnostic groups were only weakly separable, and the decision boundary tended to separate scanners rather than clinical groups. Figure 6 shows a representation of the decision-boundary. The figure shows the decision-boundary (background colour) tends to separate shapes representing scanner differences (crosses and circles) rather than colours representing diagnostic differences (blue vs red). In particular, the crosses and circles are well-separated to the top right and bottom left of the figure, while the blue and red circles in the bottom left are intermingled. This devalues the accuracy of the model when using to predict unseen cases and typically favors the prediction of the scanner bias rather than the attributes of the disease.

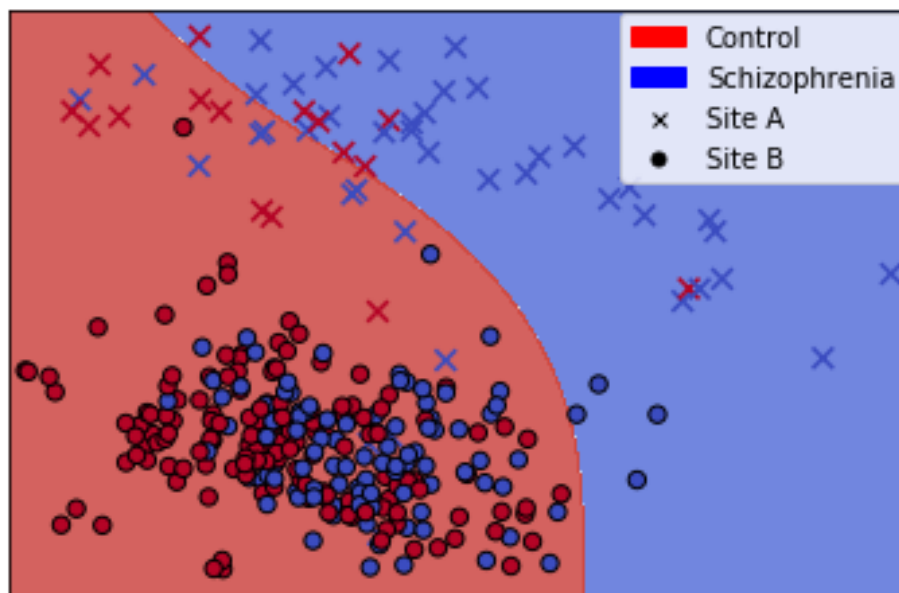


Figure 6: The decision boundary, plotted in 2D, learned by a polynomial SVM when classifying diagnostic groups. The background colour represents the decision boundary. The colour of points represents the true diagnostic group membership, and the shape of points represents the scanners.

We evaluated the ability of our generative adversarial network to remove the scanner bias in our dataset. We used the mid-sagittal slice from the T1-weighted

MRI of healthy subjects from site A and site B, and we merged the distribution of each image set by transforming the images from site A into images that have similar morphological scanner artifacts as site B. Figure 7 shows a number of examples from the different sets and their resulting transformations. The transformed images (second row) demonstrate more consistency compared to the corresponding original images (top row) and is comparable to the consistency of images from site B (bottom row). The differences between the original and transformed images, highlighted in the third row show significant changes in regions such as the thalamus and the brain stem.

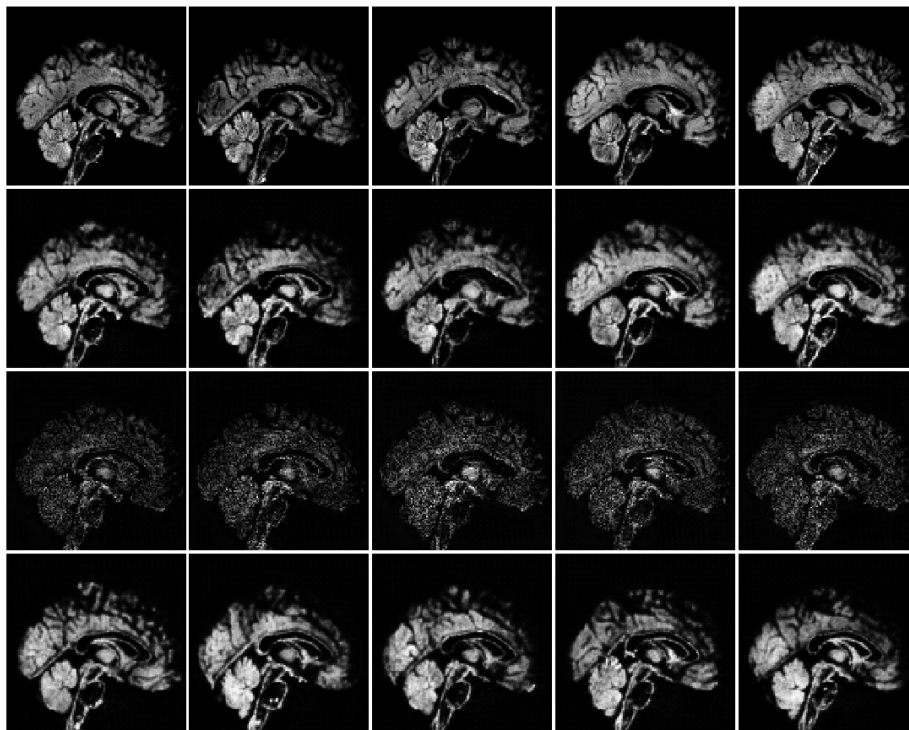


Figure 7: **Top row**: Samples of images from site A. **Second row**: The result of the transformation of images from the top row using GAN. **Third row**: The absolute difference between the images of first and second row. **Bottom row**: Samples of images from site B.

We next conducted a supervised classification test of the dataset to determine how well the images from each site were distinguishable. A Gaussian SVM

model was trained using data from healthy controls. Table 3 shows the performance of the classifier after different correctional techniques were applied to the healthy dataset, including linear regression, Gaussian regression, and our GAN model. The SVM was able to achieve close to 100 percent accuracy when discriminating between the two scanners without any correction (99.3% accuracy, 99.4% precision, 99.3% recall and 100% specificity). The linear correction method produced the worst outcome as the SVM was able to distinguish between the two site images with 100% accuracy after application of this method. By contrast, the non-linear correction methods such as the GAN and GP regression reduced the model’s ability to distinguish between the sites. This suggests that the non-linear correction methods remove or minimise the scanner biases present in our dataset, with the GAN correction producing the largest difference.

Table 3: Classification of scanners, using different correctional methods. Average difference in performance from baseline (no correction) across 10-fold cross-validation. Bold indicates the best performing in the category. * $p < .05$ compared to baseline.

Correction method	Accuracy	Precision	Recall	Specificity
Linear regression	0.007 [0.343]	0.006 [0.343]	0.007 [0.343]	0.000 [0.343]
GP regression	-0.309 [0.000]*	-0.476 [0.000]*	-0.309 [0.0039]*	-0.049 [0.038]*
GAN	-0.386 [0.000]*	-0.389 [0.000]*	-0.386 [0.000]*	-0.255 [0.000]*

3.2. Experiment 1b: Unsupervised classification test of scanner

We performed unsupervised learning to determine whether any unstructured information related to site differences remained in the dataset. Figure 8 shows a 2D visualisation of the differences between data sets before and after the transformation of the GAN, using two dimensionality reduction techniques: principal component analysis (PCA) and t-Distributed Stochastic Neighbor Embedding (t-SNE) (Maaten & Hinton, 2008). t-SNE, unlike PCA, is a non-linear method that is useful for exploring local neighbourhoods and finding clusters in data. If data is naively pooled (left column), there is clear separation between the

datasets from each site, suggesting that these site artifacts are a possible confound and will make any interpretation of results using pooled data difficult. However, after the GAN transformation (right column), such separation has vanished and the data is akin to that generated from the same distribution.

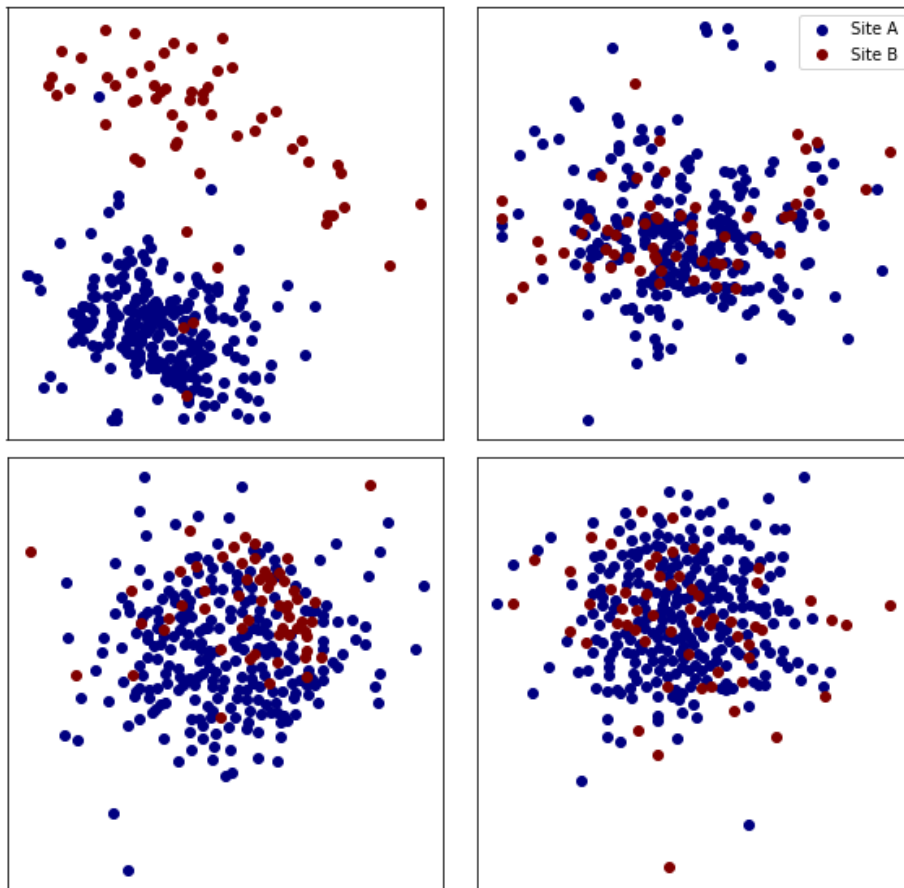


Figure 8: **Left column:** Images before transformation. **Right column:** Images after GAN transformation. **Top:** PCA visualisation of the two scanner sets. **Bottom:** a t-SNE visualisation

3.3. Experiment 2: Classification of disease

The previous experiment demonstrated the GAN correction method removed site-related information from our dataset on the basis of supervised and unsu-

pervised classification methods. An important concern is whether the information loss is selective to site differences or whether other information is also lost. To test that, we determined whether classification of clinical diagnosis was adversely affected by any of our correction methods. Gaussian kernelised version of SVM was used to classify the diagnosis of the subjects as either healthy or schizophrenia. The SVM was able to achieve over 85 percent accuracy when discriminating between the two scanners without any correction (87.1% accuracy, 89.1% precision, 87.1% recall and 95.7% specificity). Table 4 shows comparisons compared to baseline (no correction) using similar methods as in Section 3.1. Linear regression was the only method to produce negative changes in accuracy, implying it non-selectively removed information from our dataset. On the other hand, GP regression and the GAN showed significant improvements, with GAN performing best with an improved accuracy of 3.7% and 1.2% when compared to base and GP regression respectively. The negative changes in specificity after GP and GAN correction indicate there is some improvement of classification accuracy of the schizophrenia brain images at the expense of healthy brain images.

Table 4: Classification of diagnostic groups, using different correctional methods. Average difference in performance from baseline (no correction) over each cross validation fold is reported. Bold indicates the best performing in the category. Negative values indicate a worse result compared to baseline. * $p < .05$ compared to baseline.

Correction method	Accuracy	Precision	Recall	Specificity
Linear regression	-0.003 [0.726]	0.000 [0.981]	-0.003 [0.726]	0.000 [1]
GP regression	0.025 [0.038]*	0.021 [0.082]	0.026 [0.038]*	-0.042[0.143]
GAN	0.037 [0.007]*	0.028 [0.017]*	0.038 [0.007]*	-0.043[0.051]

3.4. Experiment 3: Classification of gender

The GAN correction appears to selectively remove information related to site differences in our dataset, without adversely affecting information related to

subtle clinical differences. In fact, by some metrics the GAN appears to improve diagnostic classification. However anatomical differences between psychiatric groups are likely to be small, obscure and perhaps not generally representative of the anatomical changes produced by our correction methods here. Furthermore, the contribution of diagnostic groups from each site in our dataset is unbalanced (e.g., see Table 1), and there are reasonable concerns that unbalanced sampling from confounded groups may artificially inflate classification accuracy, even after weighting for unbalanced groups (Rao et al., 2017). To help determine the general impact of our correction methods on anatomically distinct groups, and to eliminate concerns of inflated classification accuracy due to unbalanced groups, we tested the effect of GAN correction on balanced groups. We created a dataset which balanced the group contribution from each site by randomly selecting a set of 37 male images and 37 female images from each site. Thus, we balanced both gender and site in this dataset. Male and female images from each site were then pooled together, and correction methods were applied to each dataset. We then tested whether a Gaussian SVM could classify brain images by gender. On a balanced dataset, the baseline classification accuracy of the SVM (i.e., uncorrected images) was less than 70 percent (65.2% accuracy, 65.6% precision, 64.5% recall and 65.9% specificity). The results of our correction methods are shown in Table 5. The GAN corrected images improved accuracy by 15.8% compared to baseline whereas linear regression and GP regression produced no significant difference in the classification of gender from baseline (and on average they even reduced classification performance).

3.5. Experiment 4: Reconstruction

11 subjects (5 male) had undergone MRI scans at site A and site B. This allowed us to determine how similar the reconstructed images from the different methods were to images of the same brain collected at the actual site. Images from site B were corrected to site A and were compared to the actual images collected at site A for the selected subjects. The mean square error (MSE) between the corrected and actual image for each subject was calculated and was

Table 5: Classification of gender, using different correctional methods. Reported values correspond to the average of the differences of each cross validation fold test between baseline (no correction) and the correction method. Bold indicates the best performing in the category. Negative values indicate a worse result compared to baseline. $*p < .05$ compared to baseline.

Correction method	Accuracy	Precision	Recall	Specificity
Baseline	0.652	0.656	0.645	0.659
Linear regression	-0.015 [0.405]	-0.018 [0.371]	-0.016 [0.528]	-0.014 [0.343]
GP regression	-0.033 [0.087]	-0.036 [0.052]	-0.025 [0.343]	-0.041 [0.177]
GAN	0.158 [0.029]*	0.130 [0.071]	0.211 [0.006]*	0.105 [0.220]

compared to baseline. Linear regression and GP regression performed similar to each other with a 6.35% decrease in error. The GAN correction had significant improvement over the other regression methods with a 27.02% decrease in error.

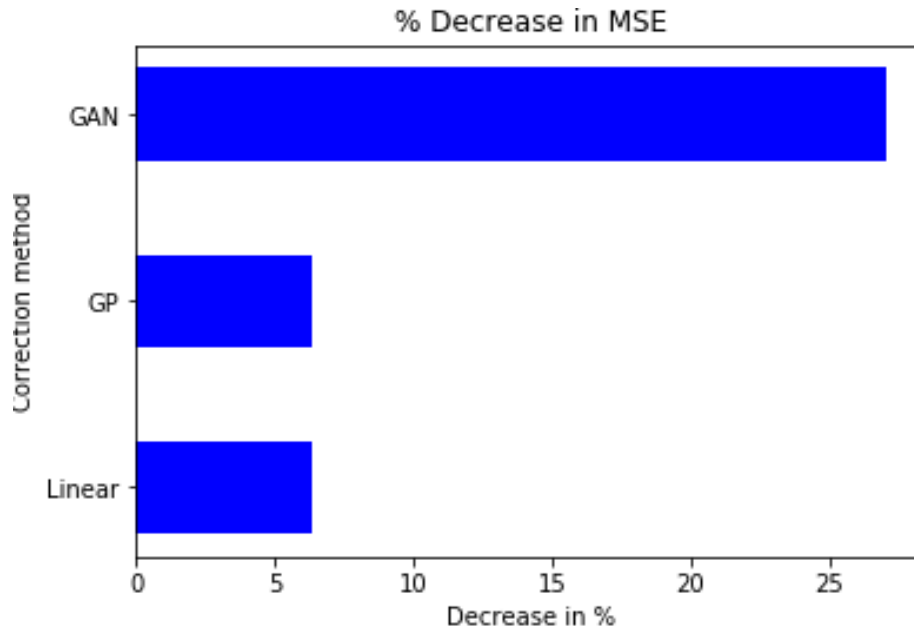


Figure 9: Percentage decrease in reconstruction (MSE) error against baseline for the different correction methods.

4. Discussion

Although combining structural MRI scans from different centres provides an opportunity to increase the statistical power of brain morphometric analyses in neurological and neuropsychiatric disorders, one important confound is the potential for scanner and MRI protocol effects to introduce systematic errors. Thus, pooling data from different sites, scanners or acquisition protocols could make the interpretation of results difficult. These MRI artifact issues are even more important with the growing popularity of automatic diagnostic systems using machine learning techniques. Although naively pooling data from multiple centres may increase sample size and intuitively, increase classification accuracy, we found that the decision boundary learned by the classifier is heavily biased towards the separating hyperplane of the scanner differences rather than the true diagnostic label (See Figure 6).

We proposed a novel method using deep learning to correct scanner biases and experimented with data from subjects suffering mental diseases such as depression and bipolar disease. The dataset was collected on two different scanners at two different sites with different hardware and protocols. As such, our dataset probably represents larger site-related differences than previous studies which used images acquired with similar MRI protocols (Kostro et al., 2014).

In comparison to other learning-based approaches, one advantage of neural networks is that no features have to be hand-crafted but instead, the model learns suitable features for the transformation during training automatically (Plis et al., 2014). In contrast to methods such as linear regression that treat voxels independently of each other, convolutional neural networks take local information into account as they are based on image patches. The fully convolutional architecture allows for a variable number of input sizes however the quality of the generation of images may change due to the fixed receptive field of the networks.

The experiments suggest that using methods such as linear regression, and in some cases GP regression (see Table 5) are not suitable to correct for scanner

artifacts as it decreases classification accuracy when discriminating diagnostic groups and still allows for differentiation between scanners. On the other hand, the GAN method here was able to capture the differences between scanners, making the transformations indistinguishable between the scanner sets and improve classification accuracy compared to baseline. This suggests that the differences in scanner artifacts are highly nonlinear that cannot be estimated using linear methods.

The small difference in performance between the GAN and GP regression when classifying diagnostic groups could be explained by the fact we only used a single sagittal slice from each brain in our dataset. A single slice would likely contain a relatively restricted amount of variance and hence represent a limit to the amount of information that can be learned from the data. The GAN correction, however, increased classification of gender significantly compared to GP regression. Figure 7 shows that most of the changes between original and transformed images occur around the thalamus and brain stem. Since the structural differences between gender occur in these regions [Ruigrok et al. \(2014\)](#) and the result of the transformation has improved the consistency of the GM maps in those regions across scanners, this allowed the classifier to learn a decision boundary that reflected gender differences rather than variation caused by scanner differences.

4.1. Limitations

The major limitation of the method described here is the restriction to 2D images. That is, the current dataset only included a single mid-sagittal slice rather than the entire MRI brain volume. Future work is planned to generalize this method to 3D datasets (e.g., MRI brain volumes). However, given the massive scientific gains offered by a valid method to pool datasets in a post-hoc manner, we also hope the details we describe here will inspire other researchers to pursue the same aim, and help any researchers currently developing a similar solution. For this reason, all data, code and models used in the present report are provided for download at [insert links here](#).

One advantage of conventional regression methods to correct confounds is that they allow for the inclusion of subject-specific covariates such as age and sex. The proposed GAN on the other hand, does not control for covariates and only learns a mapping between scanners while maintaining subject variation. Instead, these covariates must be included as a pre- or post- processing step using standard regression techniques. The inclusion of covariates within the GAN is left as future work.

References

References

- Arjovsky, M., Chintala, S., & Bottou, L. (2017). Wasserstein gan. *arXiv preprint arXiv:1701.07875*, .
- Cole, J. H., Poudel, R. P., Tsagkrasoulis, D., Caan, M. W., Steves, C., Spector, T. D., & Montana, G. (2017). Predicting brain age with deep learning from raw imaging data results in a reliable and heritable biomarker. *NeuroImage*, *163*, 115–124.
- Dukart, J., Schroeter, M. L., Mueller, K., Initiative, A. D. N. et al. (2011). Age correction in dementia—matching to a healthy brain. *PLoS one*, *6*, e22193.
- Glorot, X., & Bengio, Y. (2010). Understanding the difficulty of training deep feedforward neural networks. In *Proceedings of the Thirteenth International Conference on Artificial Intelligence and Statistics* (pp. 249–256).
- Goodfellow, I. (2016). Nips 2016 tutorial: Generative adversarial networks. *arXiv preprint arXiv:1701.00160*, .
- Ioffe, S., & Szegedy, C. (2015). Batch normalization: Accelerating deep network training by reducing internal covariate shift. *CoRR*, *abs/1502.03167*. URL: <http://arxiv.org/abs/1502.03167>. *arXiv:1502.03167*.
- Isola, P., Zhu, J.-Y., Zhou, T., & Efros, A. A. (2016). Image-to-image translation with conditional adversarial networks. *arXiv preprint arXiv:1611.07004*, .

- Jongkreangkrai, C., Vichianin, Y., Tocharoenchai, C., Arimura, H., Initiative, A. D. N. et al. (2016). Computer-aided classification of alzheimer’s disease based on support vector machine with combination of cerebral image features in mri. In *Journal of Physics: Conference Series* (p. 012036). IOP Publishing volume 694.
- Kamnitsas, K., Ledig, C., Newcombe, V. F., Simpson, J. P., Kane, A. D., Menon, D. K., Rueckert, D., & Glocker, B. (2017). Efficient multi-scale 3d cnn with fully connected crf for accurate brain lesion segmentation. *Medical image analysis*, *36*, 61–78.
- Kim, T., Cha, M., Kim, H., Lee, J., & Kim, J. (2017). Learning to discover cross-domain relations with generative adversarial networks. *arXiv preprint arXiv:1703.05192*, .
- Kingma, D., & Ba, J. (2014). Adam: A method for stochastic optimization. *arXiv preprint arXiv:1412.6980*, .
- Kleesiek, J., Urban, G., Hubert, A., Schwarz, D., Maier-Hein, K., Bendszus, M., & Biller, A. (2016). Deep mri brain extraction: a 3d convolutional neural network for skull stripping. *NeuroImage*, *129*, 460–469.
- Kostro, D., Abdulkadir, A., Durr, A., Roos, R., Leavitt, B. R., Johnson, H., Cash, D., Tabrizi, S. J., Scahill, R. I., Ronneberger, O. et al. (2014). Correction of inter-scanner and within-subject variance in structural mri based automated diagnosing. *NeuroImage*, *98*, 405–415.
- Ledig, C., Theis, L., Huszár, F., Caballero, J., Cunningham, A., Acosta, A., Aitken, A., Tejani, A., Totz, J., Wang, Z. et al. (2016). Photo-realistic single image super-resolution using a generative adversarial network. *arXiv preprint arXiv:1609.04802*, .
- Maaten, L. v. d., & Hinton, G. (2008). Visualizing data using t-sne. *Journal of Machine Learning Research*, *9*, 2579–2605.

- Magnin, B., Mesrob, L., Kinkingnéhun, S., Péligrini-Issac, M., Colliot, O., Sarazin, M., Dubois, B., Lehericy, S., & Benali, H. (2009). Support vector machine-based classification of alzheimers disease from whole-brain anatomical mri. *Neuroradiology*, *51*, 73–83.
- Mao, X., Li, Q., Xie, H., Lau, R. Y., Wang, Z., & Smolley, S. P. (2016). Least squares generative adversarial networks. *arXiv preprint ArXiv:1611.04076*, .
- Mroueh, Y., Sercu, T., & Goel, V. (2017). Mcgan: Mean and covariance feature matching gan. *arXiv preprint arXiv:1702.08398*, .
- Nowozin, S., Cseke, B., & Tomioka, R. (2016). f-gan: Training generative neural samplers using variational divergence minimization. In *Advances in Neural Information Processing Systems* (pp. 271–279).
- Payan, A., & Montana, G. (2015). Predicting alzheimer’s disease: a neuroimaging study with 3d convolutional neural networks. *arXiv preprint arXiv:1502.02506*, .
- Plis, S. M., Hjelm, D. R., Salakhutdinov, R., Allen, E. A., Bockholt, H. J., Long, J. D., Johnson, H. J., Paulsen, J. S., Turner, J. A., & Calhoun, V. D. (2014). Deep learning for neuroimaging: a validation study. *Frontiers in neuroscience*, *8*.
- Poldrack, R. A., & Gorgolewski, K. J. (2014). Making big data open: data sharing in neuroimaging. *Nature neuroscience*, *17*, 1510–1517.
- Radford, A., Metz, L., & Chintala, S. (2015). Unsupervised representation learning with deep convolutional generative adversarial networks. *arXiv preprint arXiv:1511.06434*, .
- Rao, A., Monteiro, J. M., Mourao-Miranda, J., Initiative, A. D. et al. (2017). Predictive modelling using neuroimaging data in the presence of confounds. *NeuroImage*, *150*, 23–49.

- Reed, S., Akata, Z., Yan, X., Logeswaran, L., Schiele, B., & Lee, H. (2016). Generative adversarial text to image synthesis. *arXiv preprint arXiv:1605.05396*, .
- Ruigrok, A. N., Salimi-Khorshidi, G., Lai, M.-C., Baron-Cohen, S., Lombardo, M. V., Tait, R. J., & Suckling, J. (2014). A meta-analysis of sex differences in human brain structure. *Neuroscience & Biobehavioral Reviews*, *39*, 34–50.
- Sacchet, M. D., Prasad, G., Foland-Ross, L. C., Thompson, P. M., & Gotlib, I. H. (2015). Support vector machine classification of major depressive disorder using diffusion-weighted neuroimaging and graph theory. *Frontiers in psychiatry*, *6*.
- Sarraf, S., Tofighi, G. et al. (2016). Deepad: Alzheimer s disease classification via deep convolutional neural networks using mri and fmri. *bioRxiv*, (p. 070441).
- Zhu, J.-Y., Park, T., Isola, P., & Efros, A. A. (2017). Unpaired image-to-image translation using cycle-consistent adversarial networks. *arXiv preprint arXiv:1703.10593*, .